

Spark in the Dark: Evaluating Encoder-Decoder Pairs for COVID-19 CT's Semantic Segmentation

Bruno A. Krinski, Daniel V. Ruiz, and Eduardo Todt

Department of Informatics, Federal University of Paraná (UFPR), Curitiba, PR, Brazil

{bakrinski, dvruiz, todt}@inf.ufpr.br

Abstract—With the COVID-19 global pandemic, computer-assisted diagnoses of medical images have gained a lot of attention, and robust methods of Semantic Segmentation of Computed Tomography (CT) turned highly desirable. Semantic Segmentation of CT is one of many research fields of automatic detection of Covid-19 and was widely explored since the Covid-19 outbreak. In the robotic field, Semantic Segmentation of organs and CTs are widely used in robots developed for surgery tasks. As new methods and new datasets are proposed quickly, it becomes apparent the necessity of providing an extensive evaluation of those methods. To provide a standardized comparison of different architectures across multiple recently proposed datasets, we propose in this paper an extensive benchmark of multiple encoders and decoders with a total of 120 architectures evaluated in five datasets, with each dataset being validated through a five-fold cross-validation strategy, totaling 3,000 experiments. To the best of our knowledge, this is the largest evaluation in number of encoders, decoders, and datasets proposed in the field of Covid-19 CT segmentation.

I. INTRODUCTION

As of late 2019, the world faces the worst pandemic in years, with the new coronavirus disease, COVID-19, becoming a threat worldwide [1]. According to the global case count from the Systems Science and Engineering (CSSE) at Johns Hopkins University (JHU) (updated April 20th, 2021), there are a total of 196,743,788 cases identified all around the globe, with a total of 4,201,812 global deaths [2].

Early diagnosis is one of the most effective ways to fight against the virus [3], with automatic detection of Covid-19 presence in CT being highly desirable, and recent results showing effectiveness in diagnosing and identifying Covid-19 patients [4]. Semantic Segmentation [5] of CT is one of many research fields of automatic detection of Covid-19 and was widely explored since the Covid-19 outbreak [4]. In the robotic field, Semantic Segmentation of organs and CTs are widely used in robots developed for surgery tasks [6], [7].

Aiming to perform the segmentation of Covid-19 CTs, many studies apply Deep Learning techniques and Deep Neural Networks, achieving impressive results in the task [4]. Deep Neural Networks are widely applied in segmentation problems due to their great generalization capacity, learning to represent different classes of objects [8], [9].

However, with new approaches being proposed quickly, an urgency aggravated by the global pandemic, the need for an extensive evaluation becomes apparent. To provide a standardized comparison of different architectures across

multiple recently proposed datasets, we propose in this paper an extensive benchmark of multiple encoders and decoders with a total of 120 architectures evaluated. The models were trained and evaluated across five different CTs datasets: MedSeg [10], Zenodo [11], CC-CCII [12], MosMed [13], Ricord1a [14]. Each dataset was validated through a five-fold cross-validation strategy, totaling 3,000 experiments. To the best of our knowledge, this is the largest evaluation in number of encoders, decoders, and datasets proposed in the field of Covid-19 CT segmentation.

All models were trained using the same loss function to ensure baseline comparability, see section III, and without any data augmentation. The goal is to provide a lower bound estimate for each encoder-decoder combination on different datasets. A specialized study on the impact of different data augmentation techniques on each model was left for future works.

II. RELATED WORK

This section presents studies about Semantic Segmentation techniques proposed to perform segmentation of Covid-19 CT-Scans. Starting with the study presented in [15], the authors performed a comparison between U-net [16] and SegNet [17] architectures on the Covid-19 CT-Scan segmentation problem. In [18], the authors proposed a segmentation network with Reverse Attention (RAS) modules attached in the decoder side. These RA modules aim to focus on the opposite regions of the interest regions, focusing the attention on background regions instead of Covid lesion regions.

In [19], the authors modified the U-net model by replacing the decoder side's convolution layers with dilated convolutions. Also, proposed a dual attention module attached to the skip connections in the decoder module. The dual attention module comprises a Gate Attention Module (GAM) and a Decoder Attention Module (DAM). The former refine the features extracted by the encoder, and the latter reduces the semantic gap by fusing high and low-level feature maps. A module called Residual Attention Block (RAB) is attached to each block of the decoder side. In this RAB, a hybrid dilated convolution module and a DAM are integrated to refine post-upsample features.

In [20], the authors proposed a U-net-like architecture with attention modules to perform segmentation of Covid-19 lesions. Each block in the encoder and decoder has a Res_dil block after a sequence of convolutional layers. These Res_dil

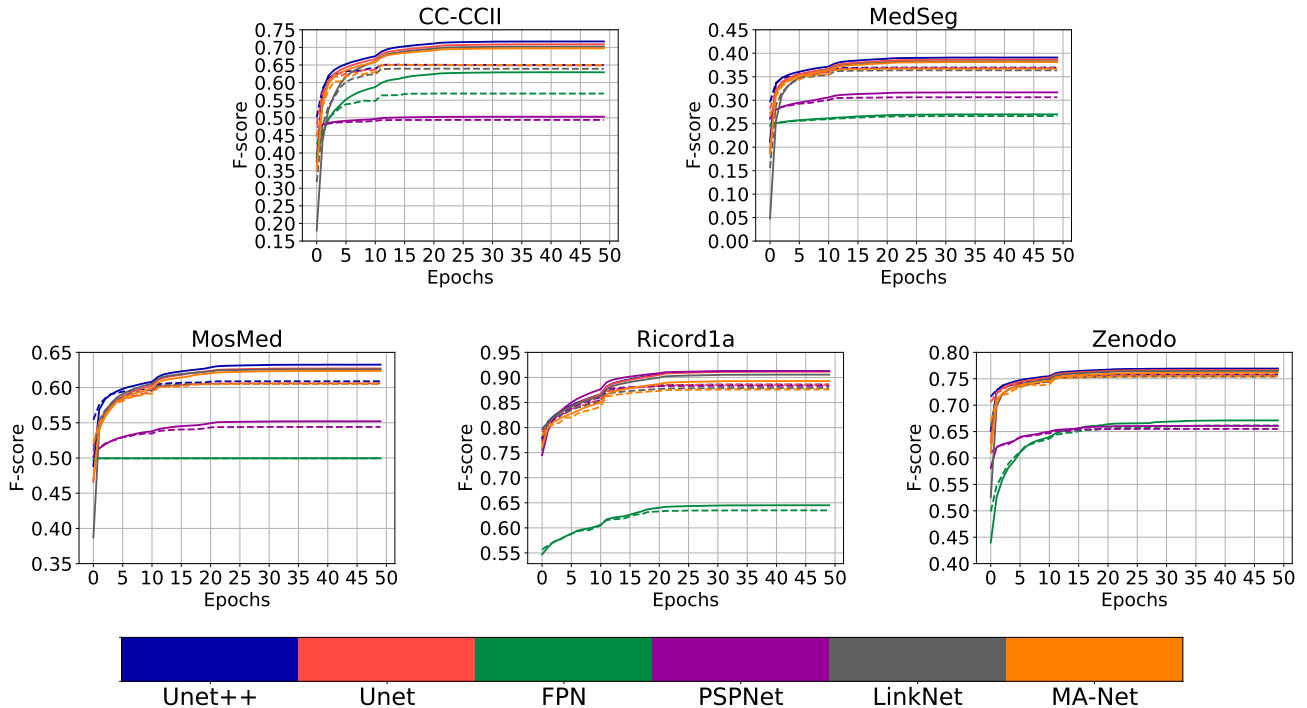


Fig. 1: The train and validation average of the k-folds F-score curves for each decoder. The filled line is the train F-score curve, and the dashed line is the validation F-score curve. Each encoder-decoder combination was trained through a five-fold cross-validation strategy. The curves are color-coded by decoder (U-Net, U-Net++, Feature Pyramid Network (FPN), Pyramid Scene Parsing Network (PSPNet), LinkNet, and Multi-scale Attention Net (MA-Net)) and represent the average F-score of the five-folds of all encoders (ResNet-50-fold0, ..., ResNet-50-fold4, ResNet-101-fold0, ..., ResNet-101-fold4, etc.) using that decoder.

blocks use dilated convolutions to help the network to learn more detailed regions of the image. Each skip connection of the U-net, which connects a convolution block to its mirror deconvolution block, has two attention mechanisms built with dilated convolutions. The first one attached at the beginning of the skip connection and another at the end.

The architecture proposed in [21] is a U-net-like model with an encoder-decoder structure. The authors proposed an Improved Dilation Convolution (IDC) module attached between the encoder and decoder to increase the receptive field and gather detailed edge information, which helps extract characteristics. An Attention Gate (AG) module is used in each skip connection between encoder and decoder mirror blocks to reduce the loss of spatial information in the feature mapping at the end of the encoder.

In [22], the authors evaluated the combination of features extracted from CT-Scans with Covid lesions and features extracted from CT-Scans with lesions from no-Covid samples. In [23], a study evaluating U-Net [16] application to the Covid CT-Scan segmentation problem is presented. All convolutional blocks of the evaluated U-net were replaced by a ResNeXt [24] block. Also, an attention mechanism was proposed to capture complex features from the feature maps. The output of each block in the decoder is concatenated with the output of an encoder block, inputs the attention mechanism, and then inputs the following decoder block.

A comparative study of networks for Covid-19 problem is presented in [25]. The authors evaluated 100 architectures in two Covid-19 CT-Scan datasets.

III. ARCHITECTURES AND DATASETS

In order to evaluate different networks in the problem of Covid-19 CT segmentation, we use networks based on encoder-decoder structure. We evaluated twenty encoders: ResNet-50 and ResNet-101 [26]; ResNeXt50 and ResNeXt101 [24]; Res2Net50 and Res2Net101 [27]; VGG16 [28]; DenseNet121, DenseNet169, and DenseNet201 [29]; Squeeze-and-Excitation Network (SE-Net)-ResNet50, SE-Net-ResNet101, SE-Net-ResNeXt50, and SE-Net-ResNeXt101 [30]; RegNetx-002, RegNetx-004, RegNetx-006, RegNety-002, RegNety-004, and RegNety-006 [31]; and six decoders: U-Net [16], U-Net++ [32], FPN [33], PSPNet [34], LinkNet [35], and Multi-scale Attention Net (MA-Net) [36]. Each encoder is combined with all decoders, resulting in a total of 120 networks evaluated.

The networks were evaluated through the F-score, see equation 2, and Intersection over Union (IoU), see equation 3, as metrics and trained with the loss function presented in equation 1:

$$Loss = 1 - \frac{w_1 * F - score + w_2 * IoU}{2} \quad (1)$$

TABLE I: The average value of five-folds cross-validation strategy for test set evaluated with the last train weight. The best F-score values are highlighted in blue and the best IoU values are highlighted in red.

Decoder	Encoder	CC-CCII		MedSeg		MosMed		Ricord1a		Zenodo	
		F-score	IoU	F-score	IoU	F-score	IoU	F-score	IoU	F-score	IoU
U-Net++	ResNet-50	0.6460	0.6068	0.3732	0.3475	0.6135	0.5880	0.8802	0.8185	0.7351	0.7065
	ResNet-101	0.6440	0.6043	0.3719	0.3464	0.6114	0.5859	0.8697	0.8061	0.7338	0.7052
	ResNeXt50_32x4d	0.6462	0.6065	0.3740	0.3479	0.6115	0.5861	0.8789	0.8172	0.7352	0.7069
	ResNeXt101_32x8d	0.6477	0.6078	0.3721	0.3464	0.6103	0.5847	0.8721	0.8092	0.7344	0.7058
	Res2Net-50_26w_4s	0.6467	0.6076	0.3744	0.3485	0.6115	0.5863	0.8776	0.8158	0.7353	0.7071
	Res2Net-101_26w_4s	0.6458	0.6061	0.3733	0.3474	0.6132	0.5876	0.8790	0.8176	0.7350	0.7066
	Vgg16	0.6482	0.6082	0.3717	0.3459	0.6160	0.5913	0.8686	0.8053	0.7357	0.7075
	Densenet-121	0.6516	0.6121	0.3756	0.3494	0.6117	0.5857	0.8873	0.8269	0.7358	0.7077
	Densenet-169	0.6505	0.6108	0.3750	0.3490	0.6123	0.5862	0.8836	0.8228	0.7354	0.7070
	Densenet-201	0.6474	0.6074	0.3743	0.3480	0.6124	0.5868	0.8814	0.8207	0.7359	0.7078
	SE-ResNet-50	0.6482	0.6076	0.3767	0.3510	0.6219	0.5969	0.8908	0.8308	0.7360	0.7078
	SE-ResNet-101	0.6457	0.6057	0.3770	0.3512	0.6205	0.5955	0.8910	0.8311	0.7358	0.7077
	SE-ResNeXt50_32x4d	0.6479	0.6076	0.3760	0.3505	0.6168	0.5927	0.8963	0.8377	0.7367	0.7091
	SE-ResNeXt101_32x4d	0.6440	0.6042	0.3763	0.3509	0.6192	0.5947	0.8963	0.8378	0.7366	0.7088
	RegNetx-002	0.6414	0.6008	0.3744	0.3486	0.6112	0.5862	0.8954	0.8369	0.7360	0.7079
	RegNetx-004	0.6384	0.5981	0.3727	0.3468	0.6127	0.5878	0.8909	0.8317	0.7364	0.7085
	RegNetx-006	0.6386	0.5991	0.3742	0.3484	0.6108	0.5860	0.8940	0.8354	0.7352	0.7069
	RegNety-002	0.6402	0.6001	0.3743	0.3486	0.6134	0.5885	0.8954	0.8368	0.7364	0.7084
	RegNety-004	0.6402	0.6007	0.3710	0.3455	0.6162	0.5907	0.8983	0.8407	0.7364	0.7086
	RegNety-006	0.6400	0.6001	0.3735	0.3476	0.6146	0.5895	0.8962	0.8378	0.7358	0.7076
U-Net	ResNet-50	0.6512	0.6105	0.3739	0.3478	0.6123	0.5868	0.8744	0.8115	0.7342	0.7052
	ResNet-101	0.6477	0.6076	0.3725	0.3462	0.6095	0.5841	0.8719	0.8087	0.7333	0.7041
	ResNeXt50_32x4d	0.6452	0.6054	0.3732	0.3474	0.6121	0.5869	0.8734	0.8108	0.7345	0.7057
	ResNeXt101_32x8d	0.6466	0.6065	0.3712	0.3452	0.6140	0.5884	0.8700	0.8068	0.7339	0.7050
	Res2Net-50_26w_4s	0.6479	0.6079	0.3727	0.3468	0.6131	0.5874	0.8755	0.8134	0.7342	0.7053
	Res2Net-101_26w_4s	0.6492	0.6086	0.3727	0.3468	0.6130	0.5876	0.8730	0.8100	0.7341	0.7051
	Vgg16	0.6428	0.6031	0.3704	0.3443	0.6156	0.5913	0.8672	0.8035	0.7351	0.7068
	Densenet-121	0.6483	0.6092	0.3726	0.3464	0.6127	0.5864	0.8835	0.8226	0.7346	0.7058
	Densenet-169	0.6489	0.6095	0.3719	0.3459	0.5899	0.5688	0.8850	0.8241	0.7343	0.7055
	Densenet-201	0.6475	0.6075	0.3721	0.3460	0.5906	0.5694	0.8794	0.8177	0.7346	0.7058
	SE-ResNet-50	0.6454	0.6057	0.3765	0.3508	0.6208	0.5958	0.8910	0.8312	0.7354	0.7070
	SE-ResNet-101	0.6493	0.6096	0.3760	0.3507	0.6209	0.5960	0.8922	0.8326	0.7357	0.7074
	SE-ResNeXt50_32x4d	0.6462	0.6058	0.3757	0.3502	0.6182	0.5941	0.8953	0.8365	0.7354	0.7072
	SE-ResNeXt101_32x4d	0.6470	0.6070	0.3772	0.3516	0.6181	0.5939	0.8961	0.8378	0.7362	0.7083
	RegNetx-002	0.6360	0.5925	0.3707	0.3447	0.6138	0.5889	0.9042	0.8482	0.7354	0.7070
	RegNetx-004	0.6369	0.5947	0.3707	0.3445	0.6107	0.5859	0.8986	0.8417	0.7344	0.7056
	RegNetx-006	0.6337	0.5937	0.3707	0.3448	0.6108	0.5862	0.8975	0.8399	0.7343	0.7055
	RegNety-002	0.6402	0.5973	0.3712	0.3452	0.6120	0.5869	0.9028	0.8461	0.7358	0.7075
	RegNety-004	0.6370	0.5963	0.3717	0.3458	0.6107	0.5865	0.8968	0.8389	0.7355	0.7071
	RegNety-006	0.6333	0.5940	0.3705	0.3448	0.6116	0.5868	0.8893	0.8296	0.7348	0.7061
FPN	ResNet-50	0.5505	0.5150	0.2478	0.2458	0.4995	0.4990	0.7282	0.6873	0.7314	0.7012
	ResNet-101	0.6313	0.5902	0.2677	0.2611	0.4995	0.4990	0.5621	0.5403	0.7303	0.6997
	ResNeXt50_32x4d	0.4737	0.4434	0.2705	0.2636	0.4995	0.4990	0.5664	0.5453	0.5507	0.5240
	ResNeXt101_32x8d	0.6329	0.5915	0.2692	0.2624	0.4995	0.4990	0.6458	0.6146	0.6310	0.6043
	Res2Net-50_26w_4s	0.6341	0.5931	0.3177	0.3013	0.4995	0.4990	0.8032	0.7515	0.7293	0.6981
	Res2Net-101_26w_4s	0.6338	0.5925	0.2765	0.2675	0.4995	0.4990	0.6343	0.6016	0.7313	0.7011
	Vgg16	0.4931	0.4546	0.2478	0.2458	0.4995	0.4990	0.4882	0.4776	0.2355	0.2241
	Densenet-121	0.6381	0.5968	0.2907	0.2792	0.4995	0.4990	0.8844	0.8231	0.7331	0.7035
	Densenet-169	0.6349	0.5942	0.2722	0.2652	0.4995	0.4990	0.8935	0.8342	0.7324	0.7028
	Densenet-201	0.6374	0.5963	0.2715	0.2644	0.4997	0.4991	0.8928	0.8337	0.7324	0.7026
	SE-ResNet-50	0.6306	0.5896	0.3176	0.3012	0.4995	0.4990	0.6524	0.6226	0.6921	0.6622
	SE-ResNet-101	0.6319	0.5902	0.2961	0.2845	0.4995	0.4990	0.6433	0.6116	0.6922	0.6624
	SE-ResNeXt50_32x4d	0.6362	0.5948	0.2478	0.2458	0.4995	0.4990	0.5705	0.5504	0.7325	0.7028
	SE-ResNeXt101_32x4d	0.4752	0.4445	0.2478	0.2458	0.4995	0.4990	0.5720	0.5525	0.7334	0.7038
	RegNetx-002	0.5380	0.5014	0.2478	0.2458	0.4995	0.4990	0.4882	0.4776	0.3639	0.3381
	RegNetx-004	0.4633	0.4324	0.2478	0.2458	0.4995	0.4990	0.5713	0.5517	0.6309	0.6038
	RegNetx-006	0.3881	0.3632	0.2478	0.2458	0.4995	0.4990	0.5711	0.5514	0.6320	0.6055
	RegNety-002	0.6152	0.5727	0.2712	0.2643	0.4995	0.4990	0.4882	0.4776	0.6834	0.6525
	RegNety-004	0.6212	0.5794	0.2478	0.2458	0.4995	0.4990	0.4882	0.4776	0.6316	0.6049
	RegNety-006	0.3117	0.2922	0.2478	0.2458	0.4995	0.4990	0.5650	0.5436	0.5331	0.5104

where:

$$F - score = \frac{TruePositive}{TruePositive + \frac{FalsePositive + FalseNegative}{2}} \quad (2)$$

and

$$IoU = \frac{intersection}{union} \quad (3)$$

The weights w_1 and w_2 were defined as 1. The benchmark

code for running these same experiments is publicly available on¹.

The models were trained and evaluated across five different CTs datasets: MedSeg [10], Zenodo [11], CC-CCII [12], MosMed [13], and Ricord1a [14]. The MedSeg was one of the first datasets proposed in the literature, being composed of 929 images and labels for four classes, with the following pixel proportion: Background (0.98563), Ground

¹<https://github.com/VRI-UFPR/SparkInTheDarkLars2021>

TABLE II: The average value of five-folds cross-validation strategy for test set evaluated with the last train weight. The best F-score values are highlighted in blue and the best IoU values are highlighted in red (Continuation of table I).

Decoder	Encoder	CC-CCII		MedSeg		MosMed		Ricord1a		Zenodo	
		F-score	IoU	F-score	IoU	F-score	IoU	F-score	IoU	F-score	IoU
PSPNet	ResNet-50	0.4822	0.4698	0.3598	0.3336	0.5201	0.5145	0.8881	0.8276	0.6192	0.5993
	ResNet-101	0.4817	0.4692	0.2942	0.2814	0.5950	0.5704	0.8858	0.8247	0.6386	0.6156
	ResNeXt50_32x4d	0.5366	0.5122	0.3161	0.2996	0.5846	0.5634	0.8917	0.8322	0.6614	0.6364
	ResNeXt101_32x8d	0.4823	0.4701	0.3616	0.3354	0.5631	0.5471	0.8901	0.8303	0.6406	0.6183
	Res2Net-50_26w_4s	0.5044	0.4872	0.3119	0.2958	0.5832	0.5623	0.8910	0.8313	0.6412	0.6190
	Res2Net-101_26w_4s	0.4822	0.4700	0.3337	0.3129	0.5620	0.5461	0.8908	0.8310	0.6612	0.6360
	Vgg16	0.4816	0.4687	0.3394	0.3159	0.5803	0.5592	0.8793	0.8171	0.7001	0.6690
	Densenet-121	0.4992	0.4831	0.2843	0.2743	0.5632	0.5470	0.8940	0.8350	0.6200	0.6004
	Densenet-169	0.4995	0.4832	0.3621	0.3358	0.5520	0.5375	0.8930	0.8337	0.6198	0.6002
	Densenet-201	0.4933	0.4788	0.3162	0.2997	0.5564	0.5414	0.8920	0.8324	0.6198	0.6001
	SE-ResNet-50	0.5420	0.5153	0.3620	0.3358	0.5831	0.5620	0.8925	0.8329	0.6411	0.6190
	SE-ResNet-101	0.5245	0.5020	0.3443	0.3215	0.5550	0.5404	0.8913	0.8315	0.6621	0.6372
	SE-ResNeXt50_32x4d	0.4832	0.4708	0.3338	0.3130	0.5428	0.5318	0.8941	0.8355	0.6623	0.6378
	SE-ResNeXt101_32x4d	0.4826	0.4702	0.3549	0.3305	0.6080	0.5815	0.8957	0.8369	0.6197	0.6003
	RegNetx-002	0.4756	0.4589	0.2478	0.2458	0.4995	0.4990	0.8418	0.7731	0.6470	0.6162
	RegNetx-004	0.4783	0.4628	0.2478	0.2458	0.4995	0.4990	0.8601	0.7944	0.5197	0.4970
	RegNetx-006	0.4800	0.4659	0.2478	0.2458	0.4995	0.4990	0.8747	0.8118	0.6364	0.6122
	RegNety-002	0.4764	0.4596	0.2478	0.2458	0.4995	0.4990	0.8451	0.7769	0.6288	0.6013
	RegNety-004	0.4799	0.4657	0.2478	0.2458	0.4995	0.4990	0.8764	0.8136	0.6170	0.5959
	RegNety-006	0.4808	0.4668	0.2478	0.2458	0.4995	0.4990	0.8788	0.8168	0.6172	0.5963
LinkNet	ResNet-50	0.6432	0.6023	0.3561	0.3288	0.6111	0.5857	0.8612	0.7960	0.7323	0.7031
	ResNet-101	0.6438	0.6030	0.3632	0.3328	0.6072	0.5817	0.8563	0.7903	0.7315	0.7018
	ResNeXt50_32x4d	0.6281	0.5878	0.3688	0.3412	0.6125	0.5868	0.8643	0.7998	0.7339	0.7051
	ResNeXt101_32x8d	0.6455	0.6049	0.3696	0.3432	0.6103	0.5843	0.8643	0.7997	0.7322	0.7029
	Res2Net-50_26w_4s	0.6448	0.6044	0.3666	0.3375	0.6096	0.5838	0.8679	0.8040	0.7323	0.7030
	Res2Net-101_26w_4s	0.6429	0.6023	0.3695	0.3431	0.6085	0.5824	0.8716	0.8078	0.7324	0.7031
	Vgg16	0.6414	0.6024	0.3715	0.3453	0.6136	0.5888	0.8647	0.8002	0.7353	0.7070
	Densenet-121	0.6142	0.5707	0.3708	0.3445	0.6076	0.5816	0.8755	0.8129	0.7331	0.7039
	Densenet-169	0.6275	0.5862	0.3629	0.3314	0.6076	0.5820	0.8730	0.8101	0.7329	0.7038
	Densenet-201	0.6353	0.5941	0.3693	0.3430	0.6056	0.5800	0.8702	0.8065	0.7332	0.7040
	SE-ResNet-50	0.6461	0.6062	0.3743	0.3482	0.6207	0.5959	0.8893	0.8288	0.7096	0.6779
	SE-ResNet-101	0.6455	0.6056	0.3753	0.3496	0.6211	0.5963	0.8895	0.8292	0.7354	0.7070
	SE-ResNeXt50_32x4d	0.6467	0.6064	0.3757	0.3500	0.6212	0.5964	0.8934	0.8339	0.7361	0.7081
	SE-ResNeXt101_32x4d	0.6449	0.6054	0.3761	0.3505	0.6213	0.5965	0.8944	0.8352	0.7361	0.7081
	RegNetx-002	0.6135	0.5704	0.3601	0.3333	0.6038	0.5793	0.8913	0.8318	0.7250	0.6926
	RegNetx-004	0.6185	0.5766	0.3671	0.3409	0.6085	0.5836	0.8935	0.8346	0.7328	0.7032
	RegNetx-006	0.6215	0.5810	0.3673	0.3415	0.6088	0.5836	0.8895	0.8296	0.7303	0.6998
	RegNety-002	0.6135	0.5705	0.3659	0.3396	0.6063	0.5808	0.8911	0.8311	0.7314	0.7011
	RegNety-004	0.6316	0.5906	0.3675	0.3411	0.6070	0.5811	0.8946	0.8357	0.7335	0.7043
	RegNety-006	0.6286	0.5884	0.3687	0.3427	0.6127	0.5869	0.8934	0.8346	0.7343	0.7053
MA-Net	ResNet-50	0.6468	0.6036	0.3682	0.3422	0.6132	0.5880	0.8691	0.8055	0.7310	0.7008
	ResNet-101	0.6448	0.6023	0.3692	0.3430	0.6109	0.5856	0.8660	0.8017	0.7306	0.7002
	ResNeXt50_32x4d	0.6461	0.6047	0.3709	0.3449	0.6133	0.5875	0.8733	0.8104	0.7315	0.7016
	ResNeXt101_32x8d	0.6462	0.6052	0.3712	0.3446	0.6086	0.5831	0.8634	0.7982	0.7313	0.7013
	Res2Net-50_26w_4s	0.6468	0.6051	0.3701	0.3438	0.6122	0.5866	0.8689	0.8053	0.7312	0.7011
	Res2Net-101_26w_4s	0.6475	0.6062	0.3669	0.3406	0.6109	0.5852	0.8741	0.8112	0.7308	0.7004
	Vgg16	0.6452	0.6047	0.3737	0.3474	0.6169	0.5923	0.8789	0.8171	0.7351	0.7067
	Densenet-121	0.6470	0.6055	0.3645	0.3381	0.6099	0.5840	0.8565	0.7907	0.7304	0.7002
	Densenet-169	0.6455	0.6039	0.3659	0.3389	0.5797	0.5599	0.8597	0.7944	0.7296	0.6990
	Densenet-201	0.6470	0.6057	0.3647	0.3383	0.6084	0.5823	0.8615	0.7965	0.7301	0.6997
	SE-ResNet-50	0.6484	0.6076	0.3759	0.3502	0.6212	0.5960	0.8819	0.8208	0.7331	0.7038
	SE-ResNet-101	0.6479	0.6075	0.3758	0.3501	0.6206	0.5956	0.8873	0.8265	0.7333	0.7041
	SE-ResNeXt50_32x4d	0.6431	0.6026	0.3751	0.3497	0.6172	0.5928	0.8918	0.8321	0.7335	0.7043
	SE-ResNeXt101_32x4d	0.6432	0.6031	0.3755	0.3498	0.6197	0.5948	0.8917	0.8323	0.7352	0.7067
	RegNetx-002	0.6402	0.5983	0.3725	0.3467	0.6130	0.5880	0.8888	0.8288	0.7345	0.7053
	RegNetx-004	0.6392	0.5987	0.3714	0.3458	0.6089	0.5844	0.8874	0.8269	0.7340	0.7048
	RegNetx-006	0.6372	0.5969	0.3721	0.3461	0.6118	0.5873	0.8817	0.8204	0.7332	0.7038
	RegNety-002	0.6440	0.6020	0.3715	0.3457	0.6105	0.5859	0.8825	0.8210	0.7336	0.7043
	RegNety-004	0.6395	0.5988	0.3713	0.3453	0.6109	0.5862	0.8835	0.8223	0.7343	0.7054
	RegNety-006	0.6351	0.5949	0.3710	0.3454	0.6101	0.5852	0.8851	0.8241	0.7330	0.7034

Glass Opacity (GGO) (0.01072), Consolidation (0.00351), and Pleural Effusion (0.0001). The Zenodo dataset, an evolution of MedSeg, is composed of 3,520 images and also has labels for four classes, with the following pixel proportion: Background (0.89893), Left Lung (0.04331), Right Lung (0.04923), and Infections (0.00852). The MosMed dataset is composed of 2,049 images, with labels for two classes, with the following pixel proportion: Background (0.99810) and GGO-Consolidation (0.00189). Ricord dataset is divided into three sets: 1a, 1b, and 1c. The set 1a is the only one with

segmentation masks and used in our work. The Ricord1a is the largest dataset, being composed of 9,166 images and has labels for two classes, with the following pixel proportion: Background (0.95295) and Infections (0.04704). We also used a sub-set of CC-CCII with segmentation masks. This sub-set is composed of 750 images and has labels for four classes, with the following pixel proportion: Background (0.87152), Lung Field (0.11691), GGO (0.00802), and Consolidation (0.00353).

IV. EXPERIMENTS

First, all datasets were divided into training and test sets, with the training set being composed of 80% of the images and the test set 20% of the images. Then, all networks were trained for 50 epochs in the training set. Transfer learning strategy was used, and the network weights were initialized with the ImageNet [37] weights. We used a batch size of 8, with the learning rate starting at 0.001 and being divided by 10 every 10 epochs. In order to evaluate only the networks, no data augmentation was applied. The input images were resized to 256x256. The scaling factor was based on the largest dimension of the image to avoid distortion, and the smallest one was padded with zeros accordingly. Each encoder-decoder combination was trained in five datasets, with each dataset being validated through a five-fold cross-validation strategy, totaling 3.000 experiments. In Fig. 1 the curves are color-coded by decoder (U-Net, U-Net++, FPN, PSPNet, LinkNet, and MA-Net) and represent the average F-score of the five-folds of all encoders (ResNet-50-fold0, ..., ResNet-50-fold4, ResNet-101-fold0, ..., ResNet-101-fold4, etc.) using that decoder.

The U-Net++, U-Net, LinkNet, and MA-Net achieved similar results, with the U-Net++ reaching the best results in most of the datasets. The FPN and PSPNet achieved the worst results. However, the PSPNet reached close results with the U-Net++ in the Ricord1a dataset. Also, all networks achieved great generalization, with the validation curve being very close to the training curve in most of the datasets. In the CC-CCII dataset, the networks did not achieve such generalization, and the validation curve is far from the train in most networks, with the PSPNet being the only network that had good generalization in this dataset.

Also, the FPN was not capable of learning the GGO-Consolidation label in the MosMed dataset. As presented in Fig. 1, both train and validation curves are straight lines with an F-score of 50%. The FPN achieved an F-score of 99% for background and 0% for lesion class. This behavior is due to the critical class imbalance present in this dataset. The number of classes in this dataset (two classes) also contributed to this result. In the Ricord1a dataset, the FPN achieved results very far from the other networks.

Table I and Table II presents the test results obtained using the average value of the five-fold cross-validation strategy performed with the last train weight. The best F-score values are highlighted in blue, and the best IoU values are highlighted in red. The U-Net, U-Net++, and MA-Net presented more stable results, with very close results between the many encoders evaluated. However, the FPN, PSPNet, and LinkNet showed to be more sensitive to the encoder change, with a higher variation on F-score and IoU. The FPN and PSPNet achieved the worst results among the decoders, while the other decoders achieved very close results.

The MedSeg was the most challenging dataset, with all networks achieving the lowest results in this dataset. However, when compared with other datasets of Covid-19 segmentation, the MedSeg dataset presents some issues like

coarse segmentation masks with the segmentation bypassing the lung region and trash markings like circles and arrows pointing to the lesion region. These issues difficult the learning process.

In order to perform a statistical analysis of the trained models, we applied the Friedman test with the null hypothesis that the models have the same distribution. We used the individual F-score value of each image in the test set to compose the distribution of each trained model. Both encoders and decoders were compared. First, for each decoder, the Friedman test was applied to verify if there is a statistical difference between the encoders trained with that decoder. Then, the Friedman test was applied again to verify if there is a statistical difference between decoders.

In both comparisons, the resulting p -value of the Friedman test was too small to represent a double variable and end up zero, so we refuse the hypothesis and affirm that there is a statistical difference between the encoders and decoders. So, besides the average F-score and IoU of each model being close, changing the encoders linked to the decoder generates a different distribution in the test images..

V. CONCLUSION

As expected, there is no definitive answer for which encoder-decoder combination is the best to be applied in the approached problem. This study provides as the main contribution a robust guideline for future works as encoder-decoder selection, setting of variables like the number of network parameters, and training time. In terms of decoders, the U-Net and U-Net++, widely applied in the literature, achieved impressive results. However, the LinkNet and the MA-Net achieved very close results to them. Also, the FPN and PSPNet presented the worst results, appearing to be unsuitable for this problem. In terms of encoders, the performance varied depending on decoder combination and dataset applied. In general, they achieved close results, with none of them standing out.

Also, this analysis revealed some weak points to be approached in future works in terms of datasets. The major problem is the critical class imbalance within the datasets, which affects the learning process of deep neural networks. Future works could investigate data augmentation and other balancing techniques to mitigate this problem.

ACKNOWLEDGMENT

The authors would like to thank the Coordination for the Improvement of Higher Education Personnel (CAPES) for the PhD scholarship. We gratefully acknowledge the founders of the publicly available datasets, the support of NVIDIA Corporation with the donation of the GPUs used for this research and the C3SL-UFPR group for the computational cluster infrastructure.

REFERENCES

- [1] C. Wang, P. W. Horby, F. G. Hayden, and G. F. Gao, "A novel coronavirus outbreak of global health concern," *The Lancet*, vol. 395, no. 10223, pp. 470–473, Feb. 2020.

- [2] J. H. U. of Medicine, "Coronavirus resource center," <https://coronavirus.jhu.edu/>, 2021, accessed: 2021-07-30.
- [3] M. Chen, C. Tu, C. Tan, X. Zheng, X. Wang, J. Wu, Y. Huang, Z. Wang, Y. Yan, Z. Li, H. Shan, J. Liu, and J. Huang, "Key to successful treatment of covid-19: accurate identification of severe risks and early intervention of disease progression," *medRxiv*, 2020.
- [4] F. Shi, J. Wang, J. Shi, Z. Wu, Q. Wang, Z. Tang, K. He, Y. Shi, and D. Shen, "Review of artificial intelligence techniques in imaging data acquisition, segmentation, and diagnosis for COVID-19," *IEEE Reviews in Biomedical Engineering*, vol. 14, pp. 4–15, 2021.
- [5] F. Cao and Q. Bao, "A survey on image semantic segmentation methods with convolutional neural network," in *2020 International Conference on Communications, Information System and Computer Engineering (CISCE)*. IEEE, July 2020.
- [6] R. Muradore, P. Fiorini, G. Akgun, D. E. Barkana, M. Bonfe, F. Boriero, A. Caprara, G. D. Rossi, R. Dodi, O. J. Elle, F. Ferraguti, L. Gasperotti, R. Gassert, K. Mathiassen, D. Handini, O. Lambercy, L. Li, M. Kruusmaa, A. O. Manurung, G. Meruzzi, H. Q. P. Nguyen, N. Preda, G. Riolfo, A. Ristolainen, A. Sanna, C. Secchi, M. Torsello, and A. E. Yantac, "Development of a cognitive robotic system for simple surgical tasks," *International Journal of Advanced Robotic Systems*, vol. 12, no. 4, p. 37, Apr. 2015.
- [7] Q. Li, Z. Du, and H. Yu, "Precise laminae segmentation based on neural network for robot-assisted decompressive laminectomy," *Computer Methods and Programs in Biomedicine*, p. 106333, Aug. 2021.
- [8] A. Garcia-Garcia, S. Orts-Escolano, S. Oprea, V. Villena-Martinez, P. Martinez-Gonzalez, and J. Garcia-Rodriguez, "A survey on deep learning techniques for image and video semantic segmentation," *Applied Soft Computing*, vol. 70, pp. 41–65, Sept. 2018.
- [9] B. A. Krinski, D. V. Ruiz, G. Z. Machado, and E. Todt, "Masking salient object detection, a mask region-based convolutional neural network analysis for segmentation of salient objects," in *Latin American Robotics Symposium (LARS)*, 2019, pp. 55–60.
- [10] MedSeg, "Covid-19 ct segmentation dataset," <http://medicalsegmentation.com/covid19/>, 2021, accessed: 2021-05-03.
- [11] M. Jun, G. Cheng, W. Yixin, A. Xingle, G. Jiantao, Y. Ziqi, Z. Mingqing, L. Xin, D. Xueyuan, C. Shucheng, W. Hao, M. Sen, Y. Xiaoyu, N. Ziwei, L. Chen, T. Lu, Z. Yuntao, Z. Qiongie, D. Guoqiang, and H. Jian, "Covid-19 ct lung and infection segmentation dataset," 2020. [Online]. Available: <https://zenodo.org/record/3757475>
- [12] K. Zhang, X. Liu, J. Shen, Z. Li, Y. Sang, X. Wu, Y. Zha, W. Liang, C. Wang, K. Wang, L. Ye, M. Gao, Z. Zhou, L. Li, J. Wang, Z. Yang, H. Cai, J. Xu, L. Yang, W. Cai, W. Xu, S. Wu, W. Zhang, S. Jiang, L. Zheng, X. Zhang, L. Wang, L. Lu, J. Li, H. Yin, W. Wang, O. Li, C. Zhang, L. Liang, T. Wu, R. Deng, K. Wei, Y. Zhou, T. Chen, J. Y.-N. Lau, M. Fok, J. He, T. Lin, W. Li, and G. Wang, "Clinically applicable AI system for accurate diagnosis, quantitative measurements, and prognosis of COVID-19 pneumonia using computed tomography," *Cell*, vol. 181, no. 6, pp. 1423–1433, e11, June 2020.
- [13] S. Morozov, A. Andreychenko, N. Pavlov, A. Vladzimirskyy, N. Ledikhova, V. Gombolevskiy, I. Blokhin, P. Gelezhe, A. Gonchar, and V. Chernina, "MosMedData: Chest CT scans with COVID-19 related findings dataset," May 2020. [Online]. Available: <https://doi.org/10.1101/2020.05.20.20100362>
- [14] E. Tsai, S. Simpson, M. P. Lungren, M. Hershman, L. Roshkovan, E. Colak, B. J. Erickson, G. Shih, A. Stein, J. Kalpathy-Cramer, J. Shen, M. A. Hafez, S. John, P. Rajiah, B. P. Pogatchnik, J. T. Mongan, E. Altinmakas, E. Ranschaert, F. C. Kitamura, L. Topff, L. Moy, J. P. Kanne, and C. C. Wu, "Medical imaging data resource center - rsna international covid radiology database release 1a - chest ct covid+ (midrc-ricord-1a)," 2020. [Online]. Available: <https://wiki.cancerimagingarchive.net/x/DoDTB>
- [15] A. Saood and I. Hatem, "COVID-19 lung CT image segmentation using deep learning methods: U-net versus SegNet," *BMC Medical Imaging*, vol. 21, no. 1, Feb. 2021.
- [16] O. Ronneberger, P. Fischer, and T. Brox, "U-net: Convolutional networks for biomedical image segmentation," in *Lecture Notes in Computer Science*. Springer International Publishing, 2015, pp. 234–241.
- [17] V. Badrinarayanan, A. Kendall, and R. Cipolla, "SegNet: A deep convolutional encoder-decoder architecture for image segmentation," *IEEE Transactions on Pattern Analysis and Machine Intelligence*, vol. 39, no. 12, pp. 2481–2495, Dec. 2017.
- [18] D.-P. Fan, T. Zhou, G.-P. Ji, Y. Zhou, G. Chen, H. Fu, J. Shen, and L. Shao, "Inf-net: Automatic COVID-19 lung infection segmentation from CT images," *IEEE Transactions on Medical Imaging*, vol. 39, no. 8, pp. 2626–2637, Aug. 2020.
- [19] X. Zhao, P. Zhang, F. Song, G. Fan, Y. Sun, Y. Wang, Z. Tian, L. Zhang, and G. Zhang, "D2a u-net: Automatic segmentation of covid-19 lesions from ct slices with dilated convolution and dual attention mechanism," 2021.
- [20] T. Zhou, S. Canu, and S. Ruan, "Automatic COVID -19 CT segmentation using u-net integrated spatial and channel attention mechanism," *International Journal of Imaging Systems and Technology*, vol. 31, no. 1, pp. 16–27, Nov. 2020.
- [21] A. N. J. Raj, H. Zhu, A. Khan, Z. Zhuang, Z. Yang, V. G. V. Mahesh, and G. Karthik, "ADID-UNET—a segmentation model for COVID-19 infection from lung CT scans," *PeerJ Computer Science*, vol. 7, p. e349, Jan. 2021.
- [22] Y. Zhang, Q. Liao, L. Yuan, H. Zhu, J. Xing, and J. Zhang, "Exploiting shared knowledge from non-covid lesions for annotation-efficient covid-19 ct lung infection segmentation," 2020.
- [23] X. Chen, L. Yao, and Y. Zhang, "Residual attention u-net for automated multi-class segmentation of covid-19 chest ct images," 2020.
- [24] S. Xie, R. Girshick, P. Dollar, Z. Tu, and K. He, "Aggregated residual transformations for deep neural networks," in *2017 IEEE Conference on Computer Vision and Pattern Recognition (CVPR)*. IEEE, July 2017.
- [25] P. Bizopoulos, N. Vretos, and P. Daras, "Comprehensive comparison of deep learning models for lung and covid-19 lesion segmentation in ct scans," 2021.
- [26] K. He, X. Zhang, S. Ren, and J. Sun, "Deep residual learning for image recognition," in *2016 IEEE Conference on Computer Vision and Pattern Recognition (CVPR)*. IEEE, June 2016.
- [27] S.-H. Gao, M.-M. Cheng, K. Zhao, X.-Y. Zhang, M.-H. Yang, and P. Torr, "Res2net: A new multi-scale backbone architecture," *IEEE Transactions on Pattern Analysis and Machine Intelligence*, vol. 43, no. 2, pp. 652–662, Feb. 2021.
- [28] K. Simonyan and A. Zisserman, "Very deep convolutional networks for large-scale image recognition," 2015.
- [29] G. Huang, Z. Liu, L. V. D. Maaten, and K. Q. Weinberger, "Densely connected convolutional networks," in *2017 IEEE Conference on Computer Vision and Pattern Recognition (CVPR)*. IEEE, July 2017.
- [30] J. Hu, L. Shen, and G. Sun, "Squeeze-and-excitation networks," in *2018 IEEE/CVF Conference on Computer Vision and Pattern Recognition*. IEEE, June 2018.
- [31] I. Radosavovic, R. P. Kosaraju, R. Girshick, K. He, and P. Dollar, "Designing network design spaces," in *2020 IEEE/CVF Conference on Computer Vision and Pattern Recognition (CVPR)*. IEEE, June 2020.
- [32] Z. Zhou, M. M. R. Siddiquee, N. Tajbakhsh, and J. Liang, "UNet++: A nested u-net architecture for medical image segmentation," in *Deep Learning in Medical Image Analysis and Multimodal Learning for Clinical Decision Support*. Springer International Publishing, 2018, pp. 3–11.
- [33] T.-Y. Lin, P. Dollar, R. Girshick, K. He, B. Hariharan, and S. Belongie, "Feature pyramid networks for object detection," in *2017 IEEE Conference on Computer Vision and Pattern Recognition (CVPR)*. IEEE, July 2017.
- [34] H. Zhao, J. Shi, X. Qi, X. Wang, and J. Jia, "Pyramid scene parsing network," in *2017 IEEE Conference on Computer Vision and Pattern Recognition (CVPR)*. IEEE, July 2017.
- [35] A. Chaurasia and E. Culurciello, "LinkNet: Exploiting encoder representations for efficient semantic segmentation," in *2017 IEEE Visual Communications and Image Processing (VCIP)*. IEEE, Dec. 2017.
- [36] T. Fan, G. Wang, Y. Li, and H. Wang, "MA-net: A multi-scale attention network for liver and tumor segmentation," *IEEE Access*, vol. 8, pp. 179 656–179 665, 2020.
- [37] J. Deng, W. Dong, R. Socher, L.-J. Li, K. Li, and L. Fei-Fei, "ImageNet: A large-scale hierarchical image database," in *2009 IEEE Conference on Computer Vision and Pattern Recognition*. IEEE, June 2009.